



**Design and Implementation of a Numerical Technique to
Inform Anisotropic Hyperelastic Finite Element Models
using Diffusion-Weighted Imaging**

by Reuben H. Kraft and Amy M. Dagro

ARL-TR-5796

October 2011

NOTICES

Disclaimers

The findings in this report are not to be construed as an official Department of the Army position unless so designated by other authorized documents.

Citation of manufacturer's or trade names does not constitute an official endorsement or approval of the use thereof.

Destroy this report when it is no longer needed. Do not return it to the originator.

Army Research Laboratory

Aberdeen Proving Ground, MD 21005-5069

ARL-TR-5796

October 2011

Design and Implementation of a Numerical Technique to Inform Anisotropic Hyperelastic Finite Element Models using Diffusion-Weighted Imaging

Reuben H. Kraft and Amy M. Dagro

**Weapons and Materials Research Directorate, Protection Division, High Rate
Mechanics and Failure Branch, ARL**

REPORT DOCUMENTATION PAGE			Form Approved OMB No. 0704-0188		
Public reporting burden for this collection of information is estimated to average 1 hour per response, including the time for reviewing instructions, searching existing data sources, gathering and maintaining the data needed, and completing and reviewing the collection information. Send comments regarding this burden estimate or any other aspect of this collection of information, including suggestions for reducing the burden, to Department of Defense, Washington Headquarters Services, Directorate for Information Operations and Reports (0704-0188), 1215 Jefferson Davis Highway, Suite 1204, Arlington, VA 22202-4302. Respondents should be aware that notwithstanding any other provision of law, no person shall be subject to any penalty for failing to comply with a collection of information if it does not display a currently valid OMB control number. PLEASE DO NOT RETURN YOUR FORM TO THE ABOVE ADDRESS.					
1. REPORT DATE (DD-MM-YYYY) October 2011		2. REPORT TYPE Final		3. DATES COVERED (From - To) July 2010- July 2011	
4. TITLE AND SUBTITLE Design and Implementation of a Numerical Technique to Inform Anisotropic Hyperelastic Finite Element Models using Diffusion-Weighted Imaging			5a. CONTRACT NUMBER		
			5b. GRANT NUMBER		
			5c. PROGRAM ELEMENT NUMBER		
6. AUTHOR(S) Reuben H. Kraft and Amy M. Dagro			5d. PROJECT NUMBER AH80		
			5e. TASK NUMBER		
			5f. WORK UNIT NUMBER		
7. PERFORMING ORGANIZATION NAME(S) AND ADDRESS(ES) U.S. Army Research Laboratory ATTN: RDRL-WMP-B Aberdeen Proving Ground, MD 21005-5066			8. PERFORMING ORGANIZATION REPORT NUMBER ARL-TR-5796		
9. SPONSORING/MONITORING AGENCY NAME(S) AND ADDRESS(ES)			10. SPONSOR/MONITOR'S ACRONYM(S)		
			11. SPONSOR/MONITOR'S REPORT NUMBER(S)		
12. DISTRIBUTION/AVAILABILITY STATEMENT Approved for public release; distribution is unlimited.					
13. SUPPLEMENTARY NOTES Author email: reuben.h.kraft.civ@mail.mil					
14. ABSTRACT A novel implementation of Diffusion-Weighted Imaging (DWI) into a finite element model is presented for capturing the anisotropic behavior of fibrous materials. The currently available finite element codes do not allow for the incorporation of anisotropic fiber directions that exist in biological soft tissues. The present work describes the continuum theory of transversely isotropic hyperelasticity, as well as the computational methods used to extract fiber directions from medical imaging data.					
15. SUBJECT TERMS Transverse Isotropic, Hyperelasticity, Mooney Rivlin, Diffusion Tensor Imaging(DTI), Neural Tractography					
16. SECURITY CLASSIFICATION OF:			17. LIMITATION OF ABSTRACT UL	18. NUMBER OF PAGES 30	19a. NAME OF RESPONSIBLE PERSON Reuben H. Kraft
a. REPORT Unclassified	b. ABSTRACT Unclassified	c. THIS PAGE Unclassified			19b. TELEPHONE NUMBER (Include area code) 410-278-6142

Contents

List of Figures	iv
1. Introduction	1
2. Continuum Theory of Transversely Isotropic Hyperelasticity	3
2.1 Kinematics of Finite Deformations	3
2.2 Decoupled Representation of Strain Energy	4
2.3 Uncoupled Stress Tensor	4
2.4 Uncoupled Stress Tensor for a Particular $\bar{\Psi}$	6
3. Validation of Numerical Method	8
4. An Algorithm for Linking DTI and Continuum Mechanics	9
4.1 A Scheme for Averaging Multiple Fibers.....	12
5. Application to Modeling White Matter Tissue of the Human Brain	17
6. Concluding Remarks	18
7. References	19
Distribution List	20

List of Figures

Figure 1. Using Diffusion Tensor Imaging (DTI), axonal fiber tractography can be overlaid on a finite element mesh and used to construct a transversely isotropic model. Tractography consists of complex fibers shown from (b) dorsal, (c) right lateral side and (d) posterior views.	2
Figure 2. Comparison between the finite element results and analytic solutions for three different loading conditions, (a) uniaxial, (b) strip biaxial and (c) equibiaxial.	9
Figure 3. Fiber discretization and notation definitions used throughout the report.	10
Figure 4. Schematic of the various cases that are possible when determining if a fiber segment (within a given tractography fiber) overlaps with a finite element in space.	11
Figure 5. Method used to test if a specified point is within the element. Algorithms for both tetrahedron and hexahedron elements are designed and implemented.	11
Figure 6. Method used to test if a line intersects the faces of an element for the case in which the line segment intersects the element faces, but no points in the segment reside within the element (See Case 4 in figure 4).	13
Figure 7. Depending on the fiber or mesh densities, there could be multiple fibers, or multiple fiber segments, or both existing in a single element which requires an averaging scheme.	14
Figure 8. The sum of the vectors will give an average orientation.	15
Figure 9. The global algorithm used to obtain final vector orientations for each element.	15
Figure 10. Averaging fibers which are not fully contained in the element can create a misrepresented average direction for the individual element.	16
Figure 11. DTI input data versus the assigned orientation output.	17

1. Introduction

Anisotropy is prevalent in numerous biological tissues, which are comprised of fibers, or bundles of cells aligned in a uniform direction. For example, within the white matter regions of the human brain, axons tend to form complex fiber tracts that promote anatomical connectivity and communication. The bundles of axonal fibers can be visualized using non-invasive tools such as diffusion tensor magnetic resonance medical imaging (DTI). The basic principle behind DTI is that water diffuses more rapidly in the direction aligned with the internal structure, and more slowly as it moves perpendicular to the preferred direction. From the diffusion tensor computed from the imaging, diffusion anisotropy measures such as the fractional anisotropy (FA) can further be computed. In addition, the principal direction of the diffusion tensor can be used to estimate the white matter connectivity of the brain. Visualization of the white matter connectivity is called tractography. An example of DTI tractography is shown in figure 1. Note that DTI is one particular method or application of the broader Diffusion-Weighted Imaging (DWI).

The anisotropic properties of biological tissue are important to capture within a computational framework because the axonal fiber tracts have been reported to be approximately three times stiffer than the surrounding matrix (1). In fact, numerous efforts have focused on incorporating details of fiber tractography into a computational framework where many use transversely isotropic viscoelastic constitutive models to represent the bulk and fiber mixture. For example, Margulies et al. (2) conduct experiments and optimization techniques to develop a transversely isotropic viscoelastic constitutive model for a porcine brainstem tissue sample. Wright et al. (3) present an analytical and computational model that also treats the white matter as an anisotropic, hyperelastic material using DTI to incorporate the structural orientation of the neural axons into the model. Wright et al. show that the degree of injury that is predicted in a computational model of DAI is highly dependent on the incorporation of the axonal orientation information and the inclusion of anisotropy into the constitutive model for white matter.

The work presented here extends previous efforts by using the transversely isotropic hyperelastic model formulation, and describes a new design and implementation for informing the finite element model using DTI in a three dimensional, parallel computing

framework. Besides biological materials, the algorithms described in this paper can be applied to a broad range of engineering materials, as well. For example, Kevlar armor protection systems contain fiber directions that rotate with the curvature of the surface. The finite element implementation included here sets the appropriate framework for incorporating fiber directions into finite element models used in a diverse range of applications.

In this report, we begin by describing the continuum theory behind the implementation of the transversely isotropic hyperelastic model in section 2 followed by results of a validation study of the implementation within the finite element framework in section 3. Then, section 4 presents an algorithm for linking DTI and the transverse isotropic model. Section 5 discusses an extension of the research to modeling the white matter tissue of the human brain in a three-dimensional finite element code. Then section 6 offers some concluding remarks and opportunities for future work.

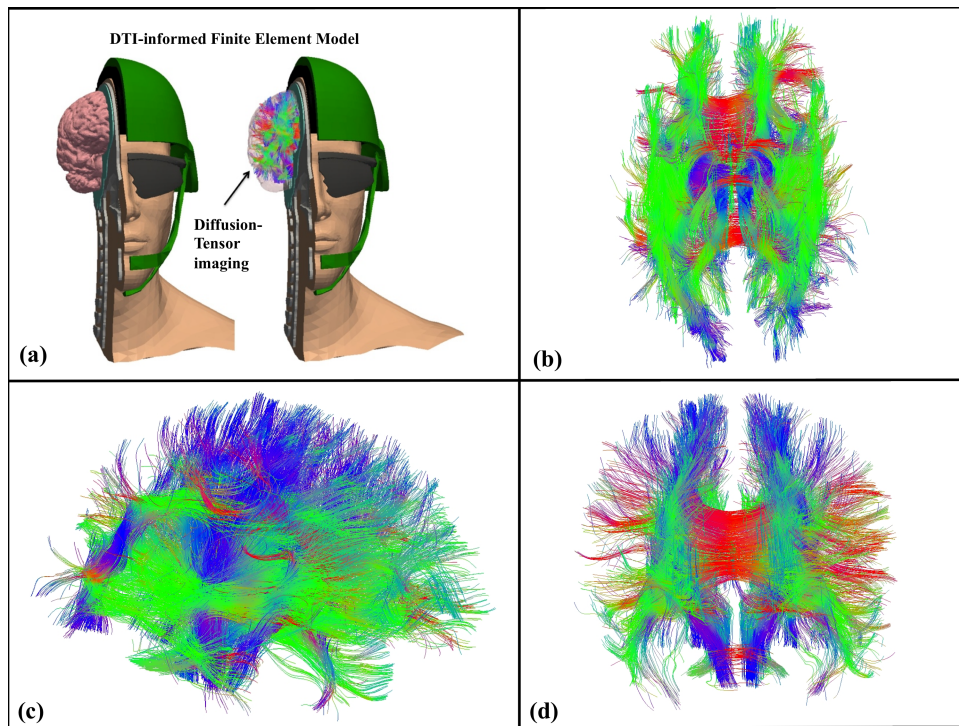


Figure 1. Using Diffusion Tensor Imaging (DTI), axonal fiber tractography can be overlaid on a finite element mesh and used to construct a transversely isotropic model. Tractography consists of complex fibers shown from (b) dorsal, (c) right lateral side and (d) posterior views.

2. Continuum Theory of Transversely Isotropic Hyperelasticity

2.1 Kinematics of Finite Deformations

We begin by defining the deformation gradient defined as:

$$\mathbf{F} = \frac{\partial \mathbf{x}}{\partial \mathbf{X}} \quad (1)$$

where \mathbf{x} is the deformed configuration of a material particle and \mathbf{X} is the reference position. The ratio of deformed to undeformed volumes is given by the determinant of \mathbf{F} ,

$$J = \det(\mathbf{F}) \quad (2)$$

Some materials behave differently in bulk and shear, so it is most beneficial to perform a multiplicative decomposition of \mathbf{F} into volume-changing (dilational) and volume-preserving (distortional) parts (4). To do this, a deviatoric deformation gradient is defined in which the volume change is eliminated:

$$\bar{\mathbf{F}} = J^{-1/3} \mathbf{F} \quad (3)$$

It then follows that:

$$\bar{\mathbf{C}} = \bar{\mathbf{F}}^T \bar{\mathbf{F}} \quad (4)$$

$$\bar{\mathbf{B}} = \bar{\mathbf{F}} \bar{\mathbf{F}}^T \quad (5)$$

where $\bar{\mathbf{C}}$ and $\bar{\mathbf{B}}$ are referred to as the modified right Cauchy-Green tensor, and the modified left Cauchy-Green tensor, respectively. The modified principle invariants of the Cauchy-Green deformation tensor are:

$$\bar{I}_1 = \text{tr } \bar{\mathbf{C}} = \text{tr } \bar{\mathbf{B}} \quad (6)$$

$$\bar{I}_2 = \frac{1}{2} \left[(\text{tr } \bar{\mathbf{C}})^2 - \text{tr} (\bar{\mathbf{C}}^2) \right] = \frac{1}{2} \left[(\text{tr } \bar{\mathbf{B}})^2 - \text{tr} (\bar{\mathbf{B}}^2) \right] \quad (7)$$

$$\bar{I}_3 = \det \bar{\mathbf{C}} = \det \bar{\mathbf{B}} \quad (8)$$

Two additional invariants are introduced in order to capture the mechanics of transverse isotropic materials:

$$\bar{I}_4 = \mathbf{a}_0 \cdot \bar{\mathbf{C}} \mathbf{a}_0 \quad (9)$$

$$\bar{I}_5 = \mathbf{a}_0 \cdot \bar{\mathbf{C}}^2 \mathbf{a}_0 \quad (10)$$

where \bar{I}_4 and \bar{I}_5 arise directly from the anisotropy and describe the properties of the fiber family and its interaction with the other material constituents. The vector \mathbf{a}_0 is introduced to describe the undeformed fiber direction where we have assumed that the only anisotropic property of the solid comes from the presence of the fibers. For a material that is reinforced by only one family of fibers, the stress at a material point depends not only on the deformation gradient \mathbf{F} , but also on that single preferred direction, which is called the fiber direction.

2.2 Decoupled Representation of Strain Energy

Following the approach taken by others (2, 4, 5) in the representation of transversely isotropic hyperelasticity, a unique decoupled representation of the strain energy function per unit volume in terms of the five invariants is given by:

$$\Psi(\bar{I}_1, \bar{I}_2, \bar{I}_3, \bar{I}_4, \bar{I}_5) = \Psi_{\text{iso}}(\bar{I}_1, \bar{I}_2, \bar{I}_3) + \Psi_{\text{aniso}}(\bar{I}_4, \bar{I}_5) \quad (11)$$

where $\Psi_{\text{iso}}(\bar{I}_1, \bar{I}_2, \bar{I}_3)$ describes the response of the isotropic matrix, and $\Psi_{\text{aniso}}(\bar{I}_4, \bar{I}_5)$ describes the directional contribution of the fiber reinforcement. Note that for an incompressible material, $\bar{I}_3 = J^2 = 1$.

2.3 Uncoupled Stress Tensor

For a hyperelastic material, the 2nd Piola-Kirchhoff stress is derived from the strain energy as:

$$\mathbf{S} = 2 \frac{\partial \Psi}{\partial \bar{\mathbf{C}}} \quad (12)$$

$$= 2J^{-2/3} \text{DEV} \left[\frac{\partial \Psi}{\partial \bar{\mathbf{C}}}(\bar{\mathbf{C}}) \right] - p J \mathbf{C}^{-1} \quad (13)$$

where the operator $\text{DEV} [\cdot] = [\cdot] - \frac{1}{3} ([\cdot] : \bar{\mathbf{C}}) \bar{\mathbf{C}}^{-1}$ extracts the deviatoric part of a tensor in the reference configuration and $p = -\frac{\partial \Psi}{\partial J}$ is the hydrostatic pressure. Using the chain

rule, equation 13 can be further written as:

$$\mathbf{S} = 2J^{-2/3}\text{DEV} \left[\sum_{a=1-5, a \neq 3} \left(\frac{\partial \Psi}{\partial \bar{I}_a} \frac{\partial \bar{I}_a}{\partial \bar{\mathbf{C}}} \right) \right] - pJ\mathbf{C}^{-1} \quad (14)$$

where the terms $\frac{\partial \bar{I}_a}{\partial \bar{\mathbf{C}}}$ are given as:

$$\frac{\partial \bar{I}_1}{\partial \bar{\mathbf{C}}} = \mathbf{I} \quad (15)$$

$$\frac{\partial \bar{I}_2}{\partial \bar{\mathbf{C}}} = \bar{I}_1 \mathbf{I} - \bar{\mathbf{C}} \quad (16)$$

$$\frac{\partial \bar{I}_4}{\partial \bar{\mathbf{C}}} = \mathbf{a}_0 \otimes \mathbf{a}_0 \quad (17)$$

$$\frac{\partial \bar{I}_5}{\partial \bar{\mathbf{C}}} = \mathbf{a}_0 \otimes \bar{\mathbf{C}} \cdot \mathbf{a}_0 + \mathbf{a}_0 \cdot \bar{\mathbf{C}} \otimes \mathbf{a}_0 \quad (18)$$

where \mathbf{I} is a 2nd rank identity tensor.

A push-forward operation on the second Piola-Kirchhoff stress tensor \mathbf{S} to the current configuration, and a scaling with the inverse of the volume ratio, transforms equation 16 to the Cauchy stress tensor of a transversely isotropic, compressible hyperelastic material:

$$\boldsymbol{\sigma} = \frac{2}{J} \text{dev} \left[\bar{\mathbf{F}} \frac{\partial \Psi}{\partial \bar{\mathbf{C}}} \bar{\mathbf{F}}^T \right] - p\mathbf{I} \quad (19)$$

$$\boldsymbol{\sigma} = \frac{2}{J} \text{dev} \left[(\Psi_1 + \bar{I}_1 \Psi_2) \bar{\mathbf{B}} - \Psi_2 \bar{\mathbf{B}}^2 + \bar{I}_4 \Psi_4 \mathbf{a} \otimes \mathbf{a} + \bar{I}_4 \Psi_5 (\mathbf{a} \otimes \bar{\mathbf{B}} \mathbf{a} + \mathbf{a} \bar{\mathbf{B}} \otimes \mathbf{a}) \right] - p\mathbf{I} \quad (20)$$

where

$$\text{dev} [\cdot] = [\cdot] - \frac{1}{3} ([\cdot] : \mathbf{I}) \mathbf{I} \quad (21)$$

$$\Psi_i = \frac{\partial \Psi}{\partial \bar{I}_i} \quad (22)$$

$$\mathbf{a} = \mathbf{F} \mathbf{a}_0 \quad (23)$$

in which \mathbf{a} describes the configuration of \mathbf{a}_0 during the deformation.

2.4 Uncoupled Stress Tensor for a Particular $\overline{\Psi}$

Within the framework of incompressible, transversely isotropic hyperelasticity, the strain energy function can be written in the uncoupled form as:

$$\Psi(\mathbf{C}) = \Psi_{\text{vol}}(J) + \overline{\Psi}_{\text{isoc}}(\overline{\mathbf{C}}) \quad (24)$$

where $\Psi_{\text{vol}}(J)$ represents the volumetric strain energy contribution and $\overline{\Psi}_{\text{isoc}}(\overline{\mathbf{C}})$ represents the isochoric strain energy function. Following Weiss (5), the isochoric part of the strain energy can be further subdivided into separate functions associated with the modified invariants:

$$\Psi(\mathbf{C}) = \Psi_{\text{vol}}(J) + \overline{F}_1(\overline{I}_1, \overline{I}_2) + \overline{F}_2(\overline{I}_4) \quad (25)$$

with:

$$\overline{F}_1 = C_1(\overline{I}_1 - 3) + C_2(\overline{I}_2 - 3) \quad (26)$$

$$\overline{F}_2 = C_3[\exp(\overline{I}_4 - 1) - \overline{I}_4] \quad (27)$$

where C_1 , C_2 , and C_3 are constants obtained from parameter fits to experimental data. Equation 26 corresponds to a modified Mooney-Rivlin model, and equation 27 describes an exponential behavior in the fiber direction that is a characteristic of most soft tissues.

Then, similar to equation 13, the second Piola-Kirchoff stress is given by:

$$\mathbf{S} = 2J^{-2/3} \text{DEV} \left[\frac{\partial \overline{\Psi}_{\text{isoc}}(\overline{\mathbf{C}})}{\partial \overline{\mathbf{C}}} \right] - \frac{\partial \Psi_{\text{vol}}(J)}{\partial J} J \mathbf{C}^{-1} \quad (28)$$

where the partial derivative of the isochoric part is given by:

$$\frac{\partial \overline{\Psi}_{\text{isoc}}(\overline{\mathbf{C}})}{\partial \overline{\mathbf{C}}} = \left[\frac{\partial \overline{\Psi}_{\text{isoc}}(\overline{\mathbf{C}})}{\partial \overline{I}_1} + \frac{\partial \overline{\Psi}_{\text{isoc}}(\overline{\mathbf{C}})}{\partial \overline{I}_2} \overline{I}_1 \right] \mathbf{I} - \frac{\partial \overline{\Psi}_{\text{isoc}}(\overline{\mathbf{C}})}{\partial \overline{I}_2} \overline{\mathbf{C}} + \frac{\partial \overline{\Psi}_{\text{isoc}}(\overline{\mathbf{C}})}{\partial \overline{I}_4} \mathbf{a}_0 \otimes \mathbf{a}_0 \quad (29)$$

so then substituting equation 29 into the DEV operator in equation 28,

$$\begin{aligned} \text{DEV} \left[\frac{\partial \overline{\Psi}_{\text{isoc}}(\overline{\mathbf{C}})}{\partial \overline{\mathbf{C}}} \right] &= \left[\frac{\partial \overline{\Psi}_{\text{isoc}}(\overline{\mathbf{C}})}{\partial \overline{I}_1} + \frac{\partial \overline{\Psi}_{\text{isoc}}(\overline{\mathbf{C}})}{\partial \overline{I}_2} \overline{I}_1 \right] \mathbf{I} - \frac{\partial \overline{\Psi}_{\text{isoc}}(\overline{\mathbf{C}})}{\partial \overline{I}_2} \overline{\mathbf{C}} + \frac{\partial \overline{\Psi}_{\text{isoc}}(\overline{\mathbf{C}})}{\partial \overline{I}_4} \mathbf{a}_0 \otimes \mathbf{a}_0 \\ &- \frac{1}{3} \left[\frac{\partial \overline{\Psi}_{\text{isoc}}(\overline{\mathbf{C}})}{\partial \overline{I}_1} \overline{I}_1 + 2 \frac{\partial \overline{\Psi}_{\text{isoc}}(\overline{\mathbf{C}})}{\partial \overline{I}_2} \overline{I}_2 + \frac{\partial \overline{\Psi}_{\text{isoc}}(\overline{\mathbf{C}})}{\partial \overline{I}_4} \overline{I}_4 \right] \mathbf{C}^{-1} \end{aligned} \quad (30)$$

Then, the second Piola-Kirchhoff stress is given by:

$$\begin{aligned} \mathbf{S} &= 2J^{-2/3} \left[\left(\frac{\partial \overline{\Psi}_{\text{isoc}}(\overline{\mathbf{C}})}{\partial \overline{I}_1} + \frac{\partial \overline{\Psi}_{\text{isoc}}(\overline{\mathbf{C}})}{\partial \overline{I}_2} \overline{I}_1 \right) \mathbf{I} - \frac{\partial \overline{\Psi}_{\text{isoc}}(\overline{\mathbf{C}})}{\partial \overline{I}_2} \overline{\mathbf{C}} + \frac{\partial \overline{\Psi}_{\text{isoc}}(\overline{\mathbf{C}})}{\partial \overline{I}_4} \mathbf{a}_0 \otimes \mathbf{a}_0 \right. \\ &\left. - \frac{1}{3} \left(\frac{\partial \overline{\Psi}_{\text{isoc}}(\overline{\mathbf{C}})}{\partial \overline{I}_1} \overline{I}_1 + 2 \frac{\partial \overline{\Psi}_{\text{isoc}}(\overline{\mathbf{C}})}{\partial \overline{I}_2} \overline{I}_2 + \frac{\partial \overline{\Psi}_{\text{isoc}}(\overline{\mathbf{C}})}{\partial \overline{I}_4} \overline{I}_4 \right) \mathbf{C}^{-1} \right] - \frac{\partial \Psi_{\text{vol}}(J)}{\partial J} J \mathbf{C}^{-1} \end{aligned} \quad (31)$$

where,

$$\frac{\partial \Psi_{\text{vol}}(J)}{\partial J} = p \quad (32)$$

$$\frac{\partial \overline{\Psi}_{\text{isoc}}(\overline{\mathbf{C}})}{\partial \overline{I}_1} = C_1 \quad (33)$$

$$\frac{\partial \overline{\Psi}_{\text{isoc}}(\overline{\mathbf{C}})}{\partial \overline{I}_2} = C_2 \quad (34)$$

$$\frac{\partial \overline{\Psi}_{\text{isoc}}(\overline{\mathbf{C}})}{\partial \overline{I}_4} = C_3 [\exp(\overline{I}_4 - 1) - 1] \quad (35)$$

Then, substituting into equation 31:

$$\begin{aligned} \mathbf{S} &= -pJ\mathbf{C}^{-1} + \\ &2J^{-2/3} [(C_1 + C_2\overline{I}_1) \mathbf{I} - C_2\overline{\mathbf{C}} + C_3 [\exp(\overline{I}_4 - 1) - 1] \mathbf{a}_0 \otimes \mathbf{a}_0 \\ &- 1/3 (C_1\overline{I}_1 + 2C_2\overline{I}_2 + C_3 [\exp(\overline{I}_4 - 1) - 1] \overline{I}_4) \mathbf{C}^{-1}] \end{aligned} \quad (36)$$

a push-forward operation yields the Cauchy stress:

$$\begin{aligned} \sigma &= -p\mathbf{I} + \\ &\frac{2}{J} [(C_1 + C_2\overline{I}_1) \overline{\mathbf{B}} - C_2\overline{\mathbf{B}}^2 + C_3 [\exp(\overline{I}_4 - 1) - 1] \mathbf{a} \otimes \mathbf{a} \\ &- 1/3 (C_1\overline{I}_1 + 2C_2\overline{I}_2 + C_3 [\exp(\overline{I}_4 - 1) - 1] \overline{I}_4) \mathbf{I}] \end{aligned} \quad (37)$$

3. Validation of Numerical Method

To insure that the stress update was properly implemented into the computational framework, numerical tests were performed and compared to an analytical solution. Single element computations of uniaxial, strip biaxial, and equibiaxial tests were performed to validate the update of the stress for the implementation against theoretical solutions. If the stresses are applied in the x-y plane along the principal axes so the σ_{zz} component is zero and the incompressibility constraint $\det \mathbf{F} = 1$ is applied, the deformation gradient can be expressed as:

$$F = \begin{bmatrix} \lambda_x & 0 & 0 \\ 0 & \lambda_y & 0 \\ 0 & 0 & \frac{1}{\lambda_x \lambda_y} \end{bmatrix} \quad (38)$$

Then using equation 37, the stresses are:

$$\sigma_{xx} = 2 \left[(C_1 + C_2 \bar{I}_1) (\bar{B}_{xx} - \bar{B}_{zz}) - C_2 (\bar{B}_{xx}^2 - \bar{B}_{zz}^2) + C_3 [\exp(\bar{I}_4 - 1) - 1] \bar{I}_4 (a_x^2 - a_z^2) \right] \quad (39)$$

$$\sigma_{yy} = 2 \left[(C_1 + C_2 \bar{I}_1) (\bar{B}_{yy} - \bar{B}_{zz}) - C_2 (\bar{B}_{yy}^2 - \bar{B}_{zz}^2) + C_3 [\exp(\bar{I}_4 - 1) - 1] \bar{I}_4 (a_y^2 - a_z^2) \right] \quad (40)$$

In the case of uniaxial extension, $\sigma_{yy} = \sigma_{zz} = 0$ and $\lambda_y = \lambda_z$. For a strip biaxial test, $\sigma_{zz} = 0$ and $\lambda_z = 1$. For an equibiaxial test, $\sigma_{zz} = 0$ and $\lambda_x = \lambda_y$. In addition, the same material constants were used for all three cases including, $C_1 = 10.0$, $C_2 = 10.0$, $C_3 = 100.0$ and $\kappa = 10.0e9$. As seen in figure 2, good agreement between the theoretical and finite element solutions for all three cases of loading is achieved. The convergence of the finite element solution to the theoretical solution demonstrates that the stress update equations were implemented correctly.

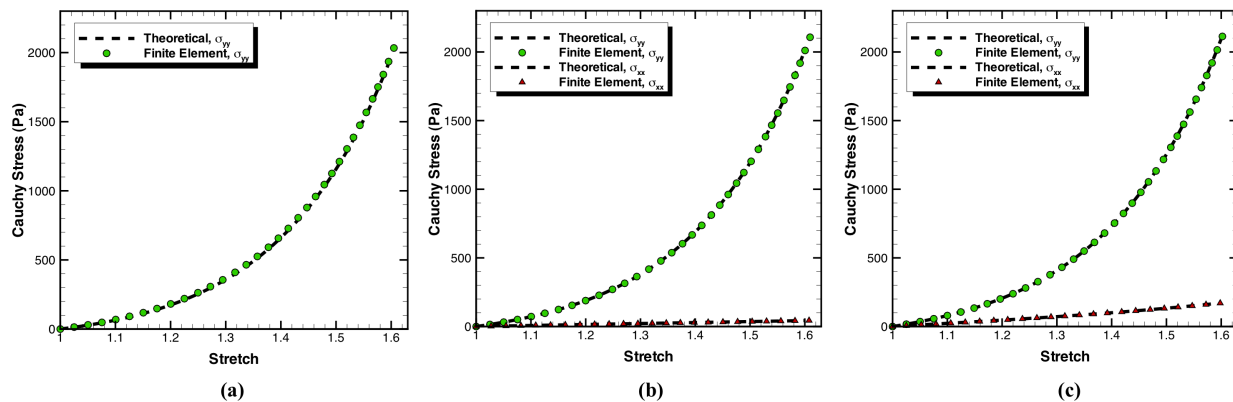


Figure 2. Comparison between the finite element results and analytic solutions for three different loading conditions, (a) uniaxial, (b) strip biaxial and (c) equibiaxial.

4. An Algorithm for Linking DTI and Continuum Mechanics

The transversely isotropic hyperelastic model previously implemented depends on the fiber reinforcement in the undeformed configuration, \mathbf{a}_0 . The algorithm developed here describes how to assign each finite element an orientation based on the fiber tractography obtained from DTI, as introduced in section 1. This is complex because of the non-linear tractography and unstructured finite element shapes within the three-dimensional framework. Algorithms for both hexahedral and tetrahedral elements are described.

First, the algorithm divides each fiber line, f_i (where i goes between 0 and the number of tractography fibers), into individual fiber segments, s_j (where j goes between 1 and the number of segments within a given fiber line). Each fiber segment consists of two fiber segment points with coordinates p_1 and p_2 : $s = p_2 - p_1$. The first discretized point within the fiber segment is assigned a direction based on the vector connecting it to the second point. If the fiber point exists at the end of a fiber line, that terminating point receives the same orientation as the previous point. A schematic of the discretization process is shown in figure 3.

Next, the algorithm determines if a fiber segment within a given tractography fiber overlaps spatially with a finite element. In order to determine this, various cases need to

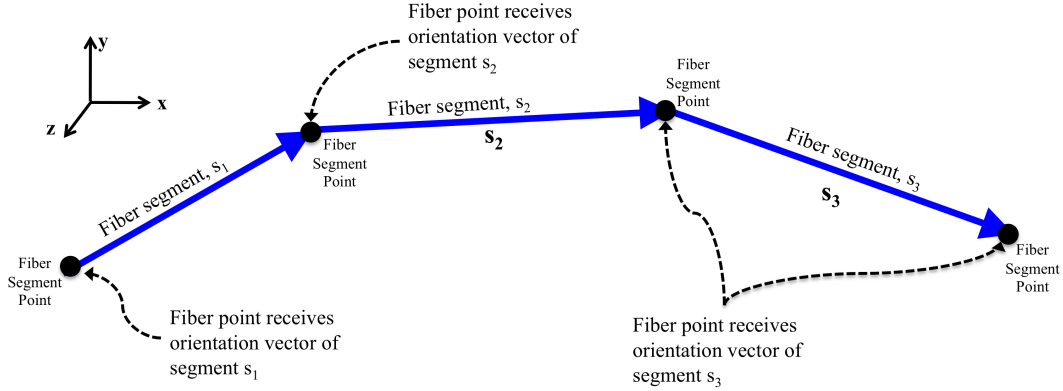


Figure 3. Fiber discretization and notation definitions used throughout the report.

be analyzed. We begin our search algorithm at the fiber segment end points. For each element in the volumetric mesh, every point within each fiber is analyzed for the cases schematically shown in figure 4. Case 1 exists if the first point in a fiber segment is contained in a given element. Case 2 exists if the second point of a fiber segment is contained in a given element. Case 3 exists if both endpoints of the fiber segment are contained within a given element. Case 4 exists if a fiber segment intersects the faces of the element, but its fiber points are not contained within a given element. Case 5 exists if the element contains none of the fiber points, and the segment does not intersect the element faces. Note, that there is an unlikely subset of case 3 when a given fiber segment lies parallel with a single element face, so this orientation would be shared by any adjacent element also.

For all of the cases shown in figure 4, determining if a fiber point is contained within a finite element is complicated by the unstructured mesh shapes. For example, in elements with adjacent faces far from orthogonal with each other, a fiber point may lie outside of the faces of the element even if the fiber point spatial coordinates are in the bounds of the maximum and minimum element nodal coordinates. Therefore, an algorithm to determine if the fiber point is inside of the element is implemented. The algorithm takes into consideration the angles of the element faces explicitly by computing normals to the element faces and the coordinates of the fiber point, as schematically shown in figure 5.

A slightly more complicated algorithm is used for case 4 where the line segment intersects the element faces, but no points in the fiber segment reside within the element.

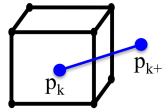
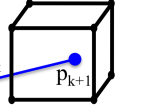
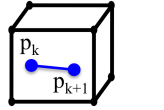
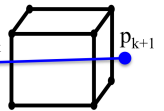
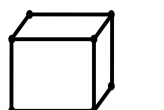
Case 1: Only the first fiber point is inside	
Case 2: Only the second fiber point is inside	
Case 3: Both fiber points are inside	
Case 4: The fiber segment crosses through the element, but no points are contained within the element	
Case 5: No fiber segments occupy space within the element	

Figure 4. Schematic of the various cases that are possible when determining if a fiber segment (within a given tractography fiber) overlaps with a finite element in space.

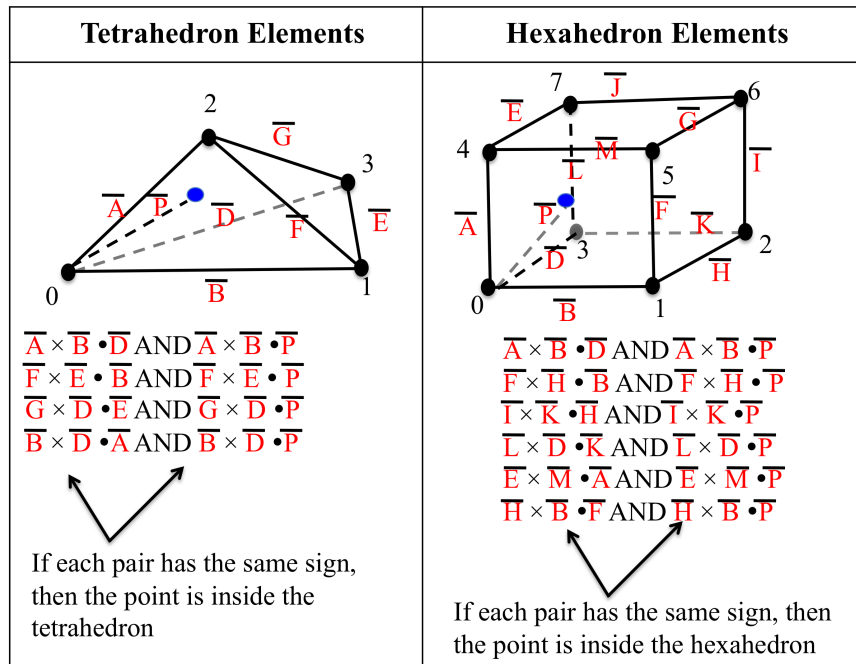


Figure 5. Method used to test if a specified point is within the element. Algorithms for both tetrahedron and hexahedron elements are designed and implemented.

As schematically shown in figure 6, first the algorithm calculates the normal of the first face, \mathbf{n} by taking the cross product of two vectors which share the same vertex, P_1 .

$$\mathbf{n} = (P_2 - P_1) \times (P_3 - P_1) \quad (41)$$

Next, the algorithm takes the dot product of the distance between an endpoint, L_1 or L_2 , and the shared vertex P_1 . This results in two dot products, the distances from L_1 and L_2 from P_1 :

$$x_1 = (L_1 - P_1) \cdot (\mathbf{n}) \quad (42)$$

$$x_2 = (L_2 - P_1) \cdot (\mathbf{n}) \quad (43)$$

If $x_1 \cdot x_2 \geq 0$, the line segment never intersects the plane of the face. If $x_1 = x_2$, the line segment and the plane are parallel, and the line segment can be disregarded since it does not intersect two different faces of the element. If the two preceding conditions do not exist, the code will find the location of the point, P , on the given line segment which intersects the plane.

$$P = L_1 + (L_2 - L_1) \left(\frac{-x_1}{x_2 - x_1} \right) \quad (44)$$

The point P is the intersection point that exists on the *plane* of the element face; therefore, the algorithm must test if P also lies within the surface area of an element face (see figure 6). A point is inside of a polygon if it is always on the same side of all the segments that create a continuous loop around the edges. For a given fiber segment that solely intersects the element faces, there should be exactly two intersection points on a single element.

If there exist elements for a given finite element mesh where no fiber tracks overlap, the elements are assigned an orientation vector of zero, $\mathbf{a}_0 = \mathbf{0}$. Therefore, the transversely isotropic material condenses to an isotropic material.

4.1 A Scheme for Averaging Multiple Fibers

The previous discussion described the methods used to find the existence and direction of a single fiber in a hexahedral or tetrahedral element. The fiber direction assigned to an element with only one fiber segment is given by:

$$\mathbf{a}_0 = \frac{\mathbf{s}}{\|\mathbf{s}\|} \quad (45)$$

First, find P, the intersection point of the line segment and plane:

Point where the line segment intersects the plane total length of line segment

$$P = L_1 + (L_2 - L_1) \left(\frac{-x_1}{x_2 - x_1} \right)$$

starting point of line segment Proportional distance from the starting point to the plane

Next, find if the point P lies within the face of the polygon:

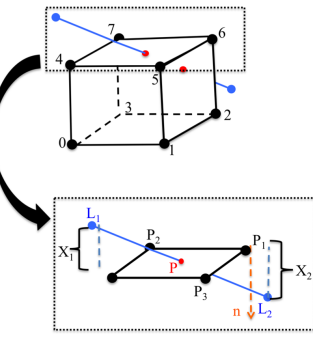
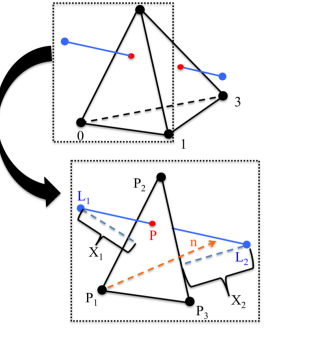
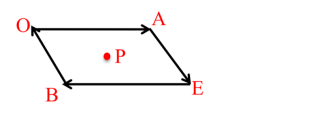
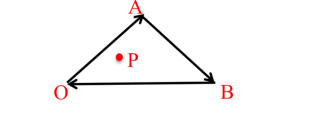
Hexahedron Elements	Tetrahedron Elements
	
	
$\begin{aligned} &(\overline{OA} \times \overline{OP}) \cdot (\overline{OA} \times \overline{OB}) \\ &(\overline{AE} \times \overline{AP}) \cdot (\overline{AE} \times \overline{AO}) \\ &(\overline{EB} \times \overline{EP}) \cdot (\overline{EB} \times \overline{EA}) \\ &(\overline{BO} \times \overline{BP}) \cdot (\overline{BO} \times \overline{BE}) \end{aligned}$	$\begin{aligned} &(\overline{OA} \times \overline{OP}) \cdot (\overline{OA} \times \overline{OB}) \\ &(\overline{AB} \times \overline{AP}) \cdot (\overline{AB} \times \overline{AO}) \\ &(\overline{BO} \times \overline{BP}) \cdot (\overline{BO} \times \overline{BA}) \end{aligned}$
<p>If all of the dot products are ≥ 0, the point, P, resides within the quadrilateral face</p>	<p>If all of the dot products are ≥ 0, the point, P, resides within the triangular face</p>

Figure 6. Method used to test if a line intersects the faces of an element for the case in which the line segment intersects the element faces, but no points in the segment reside within the element (See Case 4 in figure 4).

where s represents the orientation vector of the fiber segment. Depending on the fiber or mesh densities, there could be multiple fibers, multiple fiber segments, or both existing in a single element, as schematically depicted in figure 7. The current effort develops an average scheme for each possibility since the current implementation only permits one orientation vector per element. In future work, we hope to extend the model to have the capability to include multiple fiber orientations within a single finite element, which will require additional modifications to the theoretical basis. The method of Diffusion Spectrum Imaging (DSI) is an example of where this functionality would be useful to have, since DSI is capable of describing fiber crossings.

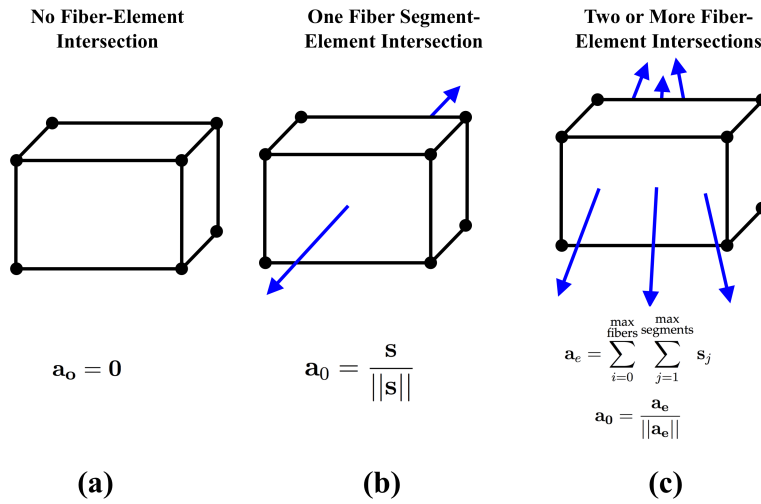


Figure 7. Depending on the fiber or mesh densities, there could be multiple fibers, or multiple fiber segments, or both existing in a single element which requires an averaging scheme.

In the case of a single fiber with multiple fiber segments within the same element, an approximation of an “average” vector direction is taken because the material model uses only one fiber direction per element. By simply adding the vectors, you obtain a resultant “average” direction, which provides an estimate of an overall fiber orientation as schematically depicted in figure 8.

For two or more fibers in a single element, the assigned orientation, \mathbf{a}_0 , is calculated by the following:

$$\mathbf{a}_e = \sum_{i=0}^{\max \text{ fibers}} \sum_{j=1}^{\max \text{ segments in fiber } i} \mathbf{s}_{[j][i]} \quad (46)$$

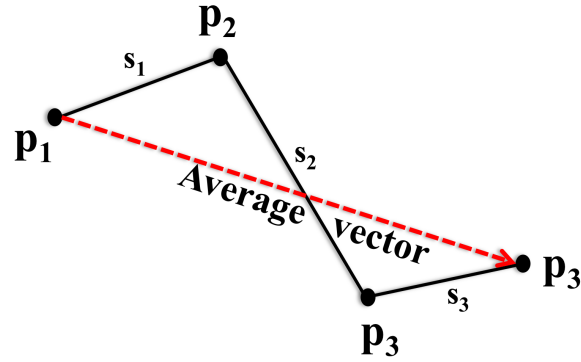


Figure 8. The sum of the vectors will give an average orientation.

$$\mathbf{a}_0 = \frac{\mathbf{a}_e}{\|\mathbf{a}_e\|} \quad (47)$$

where s_j are the orientation vectors of the fiber segments within the element, and \mathbf{a}_e represents the average of s_j – two averages are taken with each element. First, the vectors from the segments, s_j , within the same fiber line and element are averaged. Second, the average of all fibers within that element are calculated. Because the fiber average scheme depends on the element size, future efforts will explore the effects of finite element mesh density. A course finite mesh decreases computational cost, but may also smear out the complex fiber orientations. However, there are regions of the fiber tractography that change slowly over spacial distance so a course mesh may be more appropriate. The preceding procedures for determining an element orientation for the transverse isotropic model can be summarized by the global algorithm shown in figure 9.

```

for each element
  for each fiber
    for each segment in fiber
      Determine case for fiber points
      Store segment orientation vector s
    end
    Sum segment vectors for given element and fiber
  end
  Compute  $\mathbf{a}_e$  (Sum orientation vectors for all fibers in element)
  Compute  $\mathbf{a}_0$ 
end

```

Figure 9. The global algorithm used to obtain final vector orientations for each element.

Although this method will automatically take into account the vector magnitudes, one limitation of this approach involves the loss of orientation information due to the averaging scheme for adjacent fiber segments that are close to perpendicular. For example, as shown in figure 10, if one point of the fiber segment, p_1 , is entirely outside of the element, while the other point of the segment, p_2 , is inside the element but relatively close to the element's surface, that fiber segment direction will receive more weight than it should. It receives the same amount of weight as it would if it were fully contained within the element. Although the accuracy of the fiber representation is limited by the mesh resolution, it is possible in the future to create a more accurate averaging of fiber directions in each element.

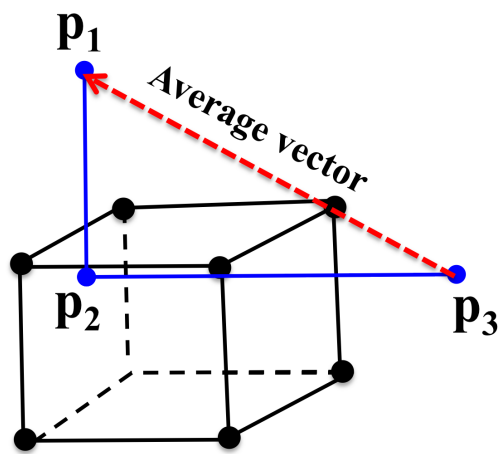


Figure 10. Averaging fibers which are not fully contained in the element can create a misrepresented average direction for the individual element.

To visualize the assigned element fiber directions, the unit vector was scaled by a characteristic length of the element (diagonal or side length) and added to the center coordinates of each element. The VTK output file describes the lines connecting the center positions and endpoints of the scaled unit vectors, which can be opened up in Paraview (Kitware) and then compared against the original dataset. The visualization lines are not meant to completely coincide with the input fiber lines but rather represent the directions assigned to each element. Since the visualization lines are positioned at the center of each element, the lines will be in close proximity to the fiber lines they represent, but will not be exactly overlapping. A higher resolution mesh will produce a more accurate representation of fiber direction assignment to the elements.

5. Application to Modeling White Matter Tissue of the Human Brain

The primary objective of implementing the transverse isotropic model was to incorporate fiber directions into the finite element models for application to anisotropic biological tissue. Multiple scenarios were created to test the algorithms; however, instead of presenting the exhaustive list here, only the brain model is shown. Figure 11a shows the input fiber tractography superimposed with a finite element mesh of the human brain. Figure 11b shows the fiber orientations assigned to the elements, obtained from the fiber tractography. While this example shows qualitative agreement, it is important to note that the finite element mesh and the fiber tractography are not from the same individual at this time. There is currently a major focus to develop models from a single individual.

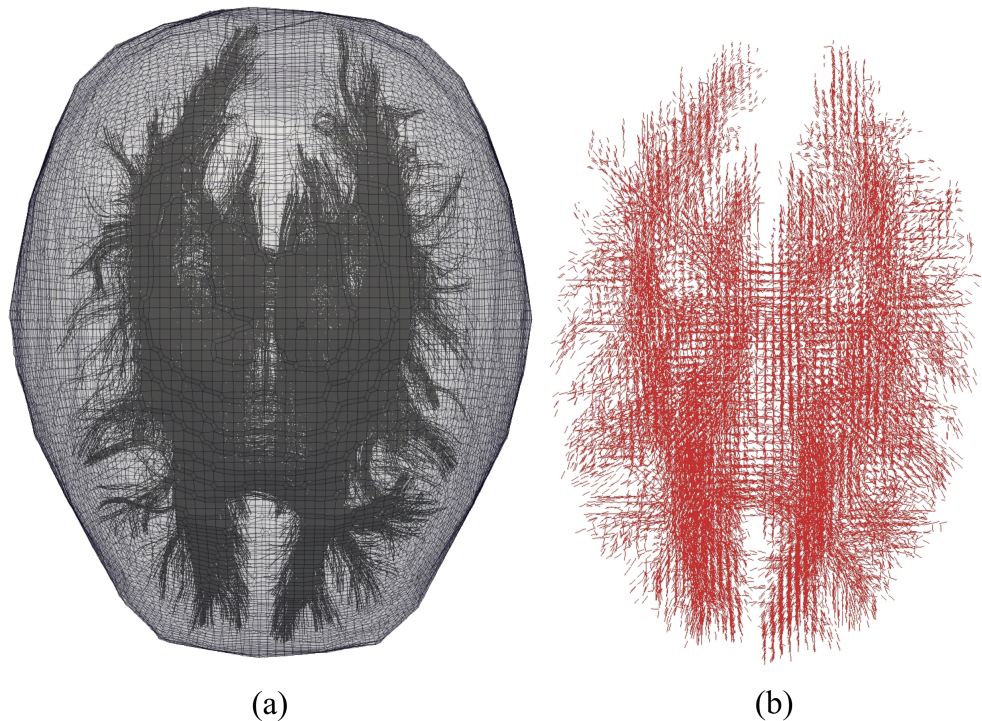


Figure 11. DTI input data versus the assigned orientation output.

6. Concluding Remarks

The work presented here provides a novel way to use state-of-the-art medical imaging to inform a 3-D transversely isotropic model of biological tissue. After testing the numerical model's implementation, an algorithm was created in order to read fiber data and output the undeformed fiber directions into the material model. The initial results are promising since they qualitatively show adequate correlation between the original DTI data and the averaged directions that were assigned to the elements. The DWI-informed modeling can be extended to other biological tissues and different material models. Aside from using DTI for imaging the white matter of the brain, it can also measure skeletal muscle fiber directions in fixated skeletal muscles. Additionally, the model could be useful for finite element modeling of non-biological fibrous materials, such as kevlar and various synthetic polymers.

As mentioned earlier, future work will include finite element models that correspond to the MRI data and DTI data derived from the same individual. The algorithm could be improved by constantly updating the fiber directions, which may change during deformation, although this would most likely increase the overall time required to run the simulation and may not be necessary for simulations of short events, such as blast or impact loading. Furthermore, DSI images may be incorporated into the computational framework so that fiber crossings may also be included.

7. References

1. Arbogast, K. B.; Margulies, S. S. A fiber-reinforced composite model of the viscoelastic behavior of the brainstem in shear. *Journal of Biomechanics* **1999**, *32* 865-870.
2. Ning, X.; Zhu, Q.; Lanir, Y.; Margulies, S. S. A Transversely Isotropic Viscoelastic Constitutive Equation for Brainstem Undergoing Finite Deformation. *Journal of Biomechanical Engineering* **2006**, *128* 925–930.
3. Wright, R.; Ramesh, K. An axonal strain injury criterion for traumatic brain injury. *Biomechanics and Modeling in Mechanobiology* **2011**, 1-16; 10.1007/s10237-011-0307-1.
4. Holzapfel, G. A. *Nonlinear Solid Mechanics*; John Wiley and Sons, LTD: 2000.
5. Weiss, J. A.; Maker, B. N.; Govindjee, S. Finite element implementation of incompressible, transversely isotropic hyperelasticity. *Computer methods in applied mechanics and engineering* **1996**, *135* 107–128.

NO. OF
COPIES ORGANIZATION

- 1 DEFENSE TECHNICAL
(PDF INFORMATION CTR
ONLY) DTIC OCA
8725 JOHN J KINGMAN RD
STE 0944
FORT BELVOIR VA 22060-6218
- 1 DIRECTOR
US ARMY RESEARCH LAB
IMNE ALC HRR
2800 POWDER MILL RD
ADELPHI MD 20783-1197
- 1 DIRECTOR
US ARMY RESEARCH LAB
RDRL CIO LL
2800 POWDER MILL RD
ADELPHI MD 20783-1197
- 1 DIRECTOR
US ARMY RESEARCH LAB
RDRL CIO MT
2800 POWDER MILL RD
ADELPHI MD 20783-1197

<u>NO. OF COPIES</u>	<u>ORGANIZATION</u>	<u>NO. OF COPIES</u>	<u>ORGANIZATION</u>
	<u>ABERDEEN PROVING GROUND</u>		K OIE
52	DIR USARL		B LANCE
	RDRL WMP		W HAIRSTON
	S SCHOENFELD		J VETTEL
	RDRL WMP F	2	DoD BLAST INJURY RESEARCH PROGRAM COORDINATING OFFICE
	N GNIAZDOWSKI		USAMRMC, ATTN: MCMR-RTB
	R KARGUS		FT. DETRICK, MD 21702-5012
	R GUPTA		M LEGGIERI
	A FRYDMAN		R GUPTA
	E FIOAVONTE		
	RDRL WMP C	1	HUMAN SYSTEMS DEPT
	T W BJERKE		CODE 4656 BLDG 2187 SUITE 2280A
	RDRL CIH C		NAVAL AIR WARFARE CENTER
	P CHUNG		AIRCRAFT DIVISION
	RDRL WML H		48110 SHAW ROAD UNIT 5
	B SCHUSTER		PATUXENT RIVER, MD 20670-1906
	RDRL WMP B		B SHENDER
	C HOPPEL		
	B LEAVY	1	AMC-TARDEC
	S R BILYK		ATTN: RDTA-RS
	D CASEM		BUILDING 200C, ROOM 1150
	J CLAYTON		WARREN, MI 48397
	D DANDEKAR		R SCHERER
	M GRINFELD		
	Y I HUANG	1	MARINA G. CARBONI
	B LOVE		NATICK SOLDIER RESEARCH DEVELOPMENT AND ENGINEERING CENTER
	M RAFTENBERG		KANSAS STREET
	M SCHEIDLER		BLDG 4, RM 247
	T WEERASOORIYA		AMSRD-NSC-WS-TB
	D POWELL		NATICK, MA 01760-5000
	A DAGRO (2 CPS)		
	D POWELL		
	M LYNCH	1	ANTON E. DMITRIEV
	S SATAPATHY		DEPARTMENT OF SURGERY, A3020
	S WOZNIAK		UNIFORMED SERVICES UNIVERSITY
	R KRAFT (10 CPS)		4301 JONES BRIDGE ROAD
	RDRL SL		BETHESDA, MD 20814
	R COATES		
	RDRL SLB W	1	ANDRZEJ J. PRZEKWAS
	W MERMAGEN		CFD RESEARCH CORPORATION
	M TEGMEYER		215 WYNN DRIVE
	C KENNEDY		HUNTSVILLE, ALABAMA 35805
	P GILLICH		
	A BREUER	1	RABIH TANNOUS
	L ROACH		BAE SYSTEMS
	R SPINK		9113 LE SAINT DRIVE
	A KULAGA		FAIRFIELD, OH 45014-5453
	N EBERIUS		
	RDRL HRS C		
	K MCDOWELL		

<u>NO. OF COPIES</u>	<u>ORGANIZATION</u>	<u>NO. OF COPIES</u>	<u>ORGANIZATION</u>
1	PHILIP DUDT NAVEL SURFACE WARFARE CENTER, CODE 664 9500 MACARTHUR DRIVE WEST BETHESDA, MD 20817	1	LAKIESHA N. WILLIAMS MISSISSIPPI STATE UNIVERSITY BOX 9632 MISSISSIPPI STATE, MS 39762
1	MICHAEL CODEGA AMC-NSRDEC KANSAS STREET NATICK, MA 01760	1	BARCLAY MORRISON COLUMBIA UNIVERSITY 351 ENGINEERING TERRACE 1210 AMSTERDAM AVENUE, MAIL CODE: 8904 NEW YORK, NY 10027
1	WAYNE STATE UNIVERSITY DIR BIOENGINEERING CENTER DEPT OF BIOMEDICAL ENGINEERING KING H. YANG 818 WEST HANCOCK DETROIT, MI 48201	1	SHANE SCHUMACHER SANDIA NATIONAL LABORATORIES NANOSCALE AND REACTIVE PROCESSES P.O. BOX 5800, MS 0836 ALBUQUERQUE, NEW MEXICO 87185-0836
2	SOUTHWEST RESEARCH INSTITUTE MECHANICAL AND MATERIALS ENGINEERING DIVISION MATERIALS ENGINEERING DEPARTMENT 6220 CULEBRA ROAD SAN ANTONIO, TX 78238 D NICOLELLA W FRANCIS	1	CHARLES E. NEEDHAM APPLIED RESEARCH ASSOCIATES INC. SOUTHWEST DIVISION 4300 SAN MATEO BLVD., NE SUITE A-220 ALBUQUERQUE, NM 87110
3	JTAPIC PROGRAM OFFICE U.S. ARMY MEDICAL RESEARCH AND MATERIAL COMMAND ATTN: MRMC-RTB 504 SCOTT STREET FORT DETRICK, MD 21702-5012 J USCLOWICZ W LEI F LEBEDA	2	ARMY RSRCH OFC RDRL ROE M D STEPP RDRL ROE V L RUSSELL PO BOX 12211 RESEARCH TRIANGLE PARK, NC 27709-2211
1	KEN L. MONSON THE UNIVERSITY OF UTAH 50 S. CENTRAL CAMPUS DRIVE 2132 MERRILL ENGINEERING BLDG SALT LAKE CITY, UTAH 84112	1	ADAM FOURNIER U.S. ARMY ABERDEEN TEST CENTER ATTN: TEDT-AT-SLB 400 COLLERAN ROAD ABERDEEN PROVING GROUND, MARYLAND 21005-5059
1	NAMAS CHANDRA UNIVERSITY OF NEBRASKA 114G OTHMER HALL P.O. BOX 880642 LINCOLN, NE 68588-0642	1	UNIV OF FLORIDA MECHL AND AEROSPACE ENGRNG G SUBHASH GAINESVILLE, FL 32611

<u>NO. OF COPIES</u>	<u>ORGANIZATION</u>	<u>NO. OF COPIES</u>	<u>ORGANIZATION</u>
5	THE JOHNS HOPKINS UNIVERSITY APPLIED PHYSICS LABORATORY 11100 JOHNS HOPKINS ROAD LAUREL, MARYLAND 20723-6099 ANDREW MERKLE MORGANA TREXLER ANDY LENNON JACK ROBERTS TIM HARRIGAN	4	DRDC VALCARTIER 2459, PIE-XI BLVD. NORTH QUEBEC, QC G3J 1X5 CANADA KEVIN WILLIAMS AMAL BOUAMOUL LUCIE MARTINEAU DENNIS NANDLALL
2	MASSACHUSETTS INSTITUTE OF TECHNOLOGY INSTITUTE FOR SOLDIER NANOTECHNOLOGIES BLDG NE47, 4TH FLOOR 77 MASSACHUSETTS AVENUE CAMBRIDGE, MA 02139 RAUL RADOVITZKY SIMONA SOCRATE	1	CRAIG BURRELL DRDC TORONTO 1133 SHEPPARD AVENUE WEST P.O. BOX 2000 TORONTO, ON M3M 3B9, CANADA
1	PAUL E. RAPP DIRECTOR, TRAUMATIC INJURY RESEARCH PROGRAM DEPARTMENT OF MILITARY AND EMERGENCY MEDICINE UNIFORMED SERVICES UNIVERSITY OF THE HEALTH SCIENCES 4301 JONES BRIDGE ROAD BETHESDA, MARYLAND 20814-4799	1	ALICE B. AIKEN CIMVHR QUEEN'S UNIVERSITY SCHOOL OF REHABILITATION THERAPY KINGSTON, ON K7L3N6, CANADA
1	JOHN M. GETZ U.S. ARMED FORCES MEDICAL EXAMINER SYSTEM 1413 RESEARCH BLVD. ROCKVILLE, MARYLAND 20850	2	CENTER FOR INJURY BIOMECHANICS WAKE FOREST UNIVERSITY MEDICAL CENTER BLVD. WINSTON-SALAM, NC 27157 JOEL STITZEL F. SCOTT GAYZIK
1	RUTGERS THE STATE UNIV OF NEW JERSEY DIR OF FED RSRCH RELATIONS B LAMATTINA 96 FRELINGHUYSEN RD CORE BLDG PISCATAWAY NJ 08854	1	DANIEL WISE HENRY JACKSON FOUNDATION U.S. ARMY AEROMEDICAL RESEARCH LABORATORY 6901 ANDREWS AVENUE FORT RUCKER, AL 36362-0577
1	ALAN HEPPER DSTL BIOMEDICAL SCIENCES RM 1A, BLDG. 245 PORTON DOWN SALISBURY, WILTSHIRE SP4 OJQ UNITED KINGDOM	1	TOM RADTKE HUMAN PROTECTION AND PERFORMANCE DIVISION DEFENCE SCIENCE AND TECHNOLOGY ORGANISATION DEPARTMENT OF DEFENCE BLDG 109, 506 LORIMER STREET FISHERMANS BEND, VICTORIA 3207 AUSTRALIA

<u>NO. OF COPIES</u>	<u>ORGANIZATION</u>	<u>NO. OF COPIES</u>	<u>ORGANIZATION</u>
2	DEPARTMENT OF MECHANICAL ENGINEERING THE JOHNS HOPKINS UNIVERSITY LATROBE 122 3400 NORTH CHARLES STREET BALTIMORE, MD 21218 K.T. RAMESH VICKY NGUYEN		
1	GARY KAMIMORI DEPARTMENT OF BEHAVIORAL BIOLOGY WALTER REED ARMY INSTITUTE OF RESEARCH 503 ROBERT GRANT AVENUE, 2W97 SILVER SPRING, MD 20910-7500		